Received: 23 April 2024 | Accepted: 11 June 2024

DOI: 10.1111/ahe.13079

SPECIAL ISSUE: ADVANCES IN APPLIED VETERINARY ANATOMY

Anatomia Histologia Embryologia

WILEY

Cone beam computed tomography and cross-sectional anatomy of the region of the fetlock in the horse (*Equus caballus*)

Jonathan Bierau[1] | **Patricia Rott**[2] | **Michael Röcken**[1] | **Carsten Staszyk**[2]

[1]Equine Clinic (Surgery, Orthopedics), Justus-Liebig-University Giessen, Giessen, Germany

[2]Faculty of Veterinary Medicine, Institute of Veterinary Anatomy, Histology and Embryology, Justus-Liebig-University Giessen, Giessen, Germany

Correspondence
Jonathan Bierau, Equine Clinic (Surgery, Orthopedics), Justus-Liebig-University Giessen, Giessen, Germany.
Email: jonathan.m.bierau@vetmed.uni-giessen.de

Abstract

This study aimed to delineate the detailed anatomy of the metacarpophalangeal (MCP) and metatarsophalangeal (MTP) joints in healthy horses using cone beam computed tomography (CBCT). The fetlock region of 15 cadaveric forelimbs and 14 cadaveric hindlimbs from nine adult horses without orthopaedic disease underwent CBCT scanning. Additionally, arthrography CBCT scans were conducted following intra-articular injection of a radiopaque contrast medium containing blue epoxy resin dye. Subsequently, limbs were frozen and sectioned to visualize anatomical structures in sectional planes corresponding to selected CBCT images. CBCT proved suitable for detailed visualization of the bony components of the fetlock region. Furthermore, the common digital extensor tendon, superficial and deep digital flexor tendons, suspensory ligament, and straight and oblique sesamoidean ligaments were identifiable on CBCT images. However, certain ligaments, such as the collateral sesamoidean ligaments and intersesamoidean ligaments, were not clearly identified. The hyaline cartilage of the MCP and MTP joint facets was assessable on the post-contrast sequence. In cases where a radiographic or ultrasound examination cannot provide a definitive diagnosis and determine the extent of disease, CBCT can provide additional valuable data on the equine MCP and MTP joint. The images obtained in this study can serve as a reference for CBCT examination of the equine MCP and MTP joint.

KEYWORDS
cone beam computed tomography, cross-sectional anatomy, diagnostic, fetlock, horse

1 | INTRODUCTION

The utilization of advanced imaging in veterinary practice, particularly in equine medicine, is expanding, with the increased availability of conventional and cone beam computed tomography (CBCT). Computed tomography (CT) plays a significant role in diagnosing orthopaedic issues in horses, providing a rapid and comprehensive understanding of the extent of disease (Bienert & Stadler, 2006). Diseases affecting the metacarpophalangeal (MCP) and metatarsophalangeal (MTP) joints commonly result in lameness in horses and have been extensively investigated with radiography and ultrasonography (Denoix et al., 1996; Ueltschi et al., 1996). However,

Michael Röcken and Carsten Staszyk are principal authors.

inconclusive results from radiography or ultrasonography have led to the necessity of cross-sectional imaging modalities like CT and MRI (Barbee et al., 1987; Bienert & Stadler, 2006; Hanson et al., 1996; Kraft & Gavin, 2001; Rijkenhuizen et al., 2005; Wisner et al., 1991). CT and MRI offer advantages over radiography and ultrasonography, including simultaneous imaging of bone and soft-tissue structures, lack of superimposition and the ability to obtain three-dimensional (3D) images through reconstruction (CT) or acquisition (MRI) (Kaneps et al., 1995; Tucker & Sande, 2001). However, these techniques also have drawbacks, such as the need for general anaesthesia and a long acquisition time (MRI), as well as high maintenance costs (Kaser-Hotz et al., 1994; Kraft & Gavin, 2001; Tucker & Sande, 2001). CT provides excellent visualization of bony structures, while MRI is better suited for assessing non-mineralized structures such as tendons, ligaments and articular cartilage (Tucker & Sande, 2001). Conventional CT scans, along with CT examinations combined with the application of intra-articular (Young et al., 2007) and intra-arterial contrast solutions (Puchalski et al., 2007), were employed to develop and outline new diagnostic techniques for assessing the equine fetlock region. However, only

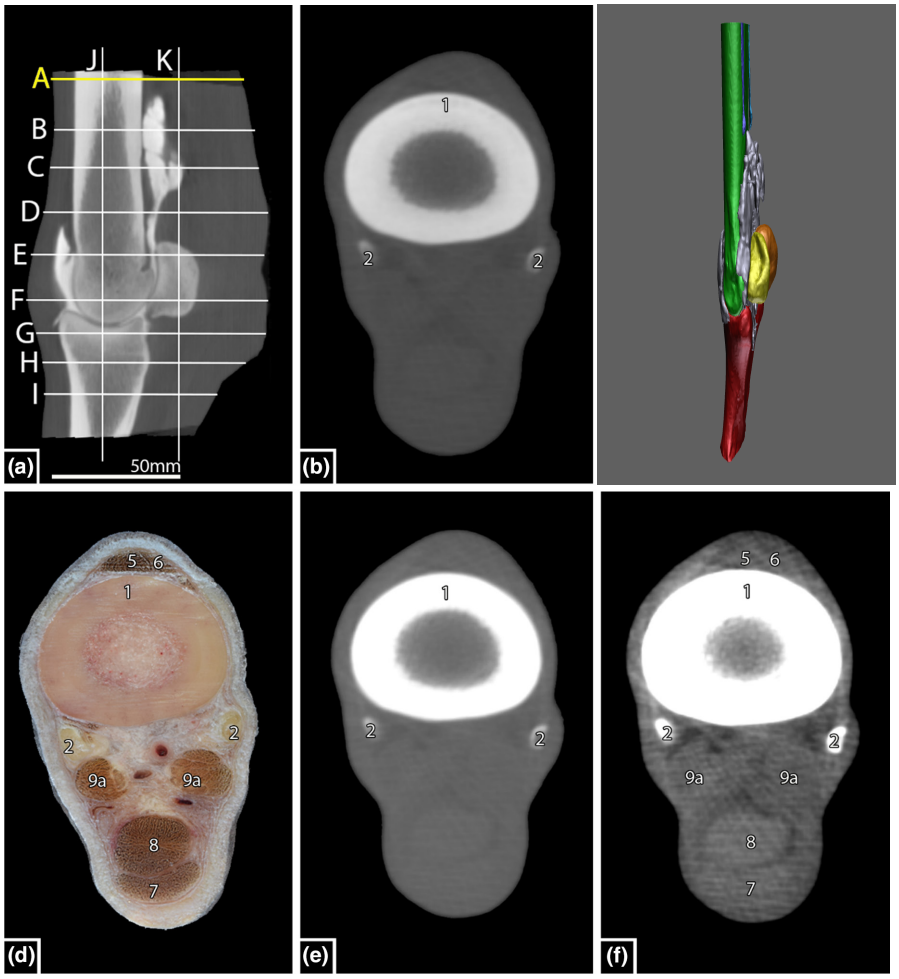

FIGURE 1 Cross-section of the fetlock joint. Illustration of the transverse sectional plane, including tendons, ligaments, and bones in the area of the distal part of the splint bone. (a) CBCT indicating the plane (yellow) displayed in (b), (d), (e) and (f). (b) Contrast medium-enhanced CBCT image. (c) Interactive 3D model of the fetlock region indicating the plane displayed in (b), (d), (e) and (f). (d) Anatomic section. (e) CBCT image, bone window. (f) CBCT image, soft tissue window. Each image is orientated with the medial aspect to the left and the dorsal aspect to the top. The choice of section was made to show the most important anatomical structures. The natural anatomical margins and functional relationships were taken into account. 1 = Third metacarpal bone (MCIII)/metatarsal bone (MTIII); 1a = Sagittal ridge of MCIII/MTIII; 1b = Collateral fossa; 2 = Second/fourth metacarpal bone (MCII/IV)/metatarsal bone (MTII/IV); 3 = Proximal sesamoid bones; 4 = Proximal phalanx; 5 = Long/common digital extensor tendon; 6 = Lateral digital extensor tendon; 7 = Superficial digital flexor tendon; 7a = Manica flexoria; 8 = Deep digital flexor tendon; 9 = Suspensory ligament; 9a = medial + lateral branch; 9b = medial + lateral extensor branch; 10 = Plantar/palmar (intersesamoidean) ligament, 10a = suprasesamoiden part, 10b = sesamoiden part; 11 = Collateral ligament; 11a = Superficial part of the collateral ligament, 11b = Deep part of the collateral ligament; 12 = Palmar annular ligament; 13 = Collateral sesamoidean ligament; 14 = Straight distal sesamoidean ligament; 15 = Oblique distal sesamoidean ligaments; 16 = Short distal sesamoidean ligaments; 17 = Cruciate distal sesamoidean ligaments; 18 = Proximopalmar/plantar recess of the metacarpophalangeal joint; 19 = Dorsal recess of the metacarpophalangeal joint; 20 = Distopalmar/plantar recess of the metacarpophalangeal joint; 21 = Cartilage of the third metacarpal bone (MCIII)/metatarsal bone (MTIII); 22 = Cartilage of the proximal sesamoid bones; 23 = Cartilage of the proximal phalanx; 24 = Joint capsule, 24a = Proximodorsal fibrosynovial plica.

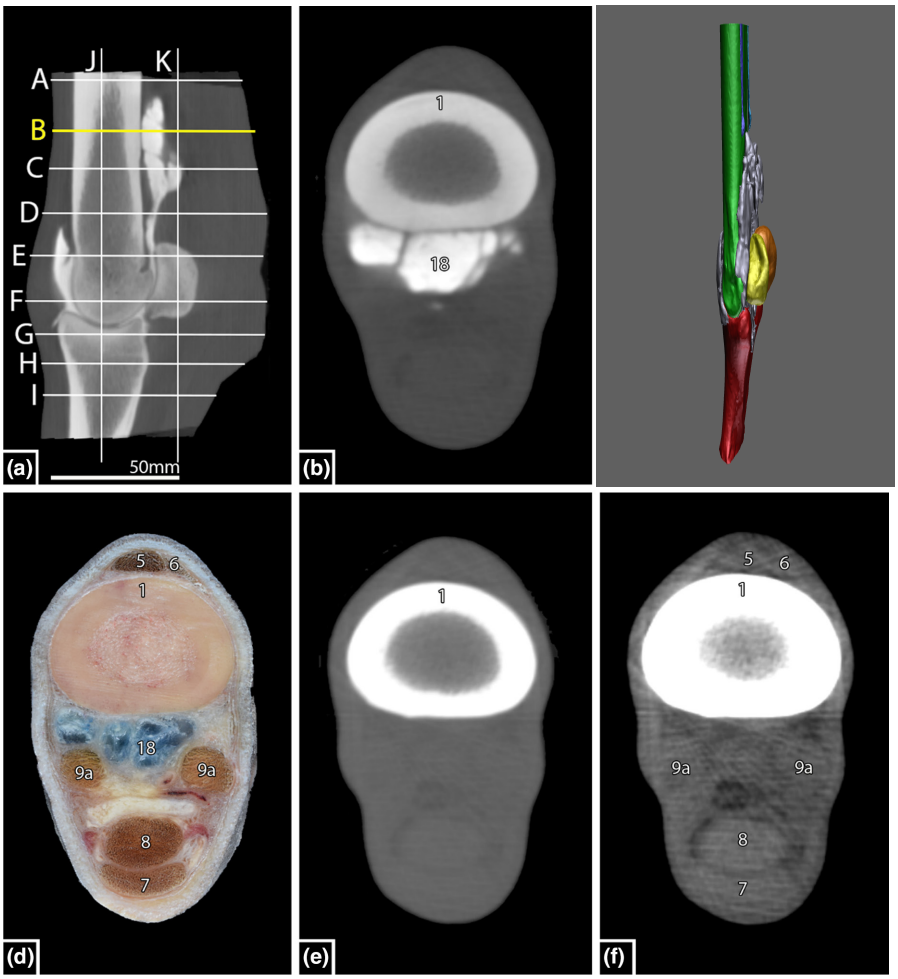

FIGURE 2 Cross-section of the fetlock joint. Illustration of the transverse sectional plane, including tendons, ligaments and bones in the area of the proximal part of the proximopalmar recess of the metacarpophalangeal joint. For further details, refer to the caption of Figure 1.

in 2008 has a description of the normal CT anatomy of the equine fetlock region been published to provide a fundamental basis for the interpretation of related CT findings (Vanderperren et al., 2008).

Recently, CBCT has gained attention in equine medicine for advanced imaging, and its utility in equine patients has been recognized (Stewart et al., 2021). However, there is currently no description of the appearance of unchanged, clinically relevant structures of the equine fetlock region displayed on CBCT images. Therefore, the objective of the present study was to provide an atlas of the CBCT anatomy of the normal equine MCP and MTP joints, with and without contrast arthrography.

2 | MATERIALS AND METHODS

2.1 | Specimens

Fifteen cadaveric forelimbs and 14 cadaveric hindlimbs from nine adult horses euthanized for reasons unrelated to this study at the Clinic for Horses (Surgery, Orthopaedics) and (Internal Medicine), Faculty of Veterinary Medicine, Justus-Liebig-University in Giessen were utilized. Within 1 h of euthanasia, the limbs were disarticulated at the level of the carpal or tarsal joint. Each limb underwent post-mortem examination through macroscopic inspection and palpation, followed by radiographic evaluation of the fetlock joints using various projections (dorso-palmar/plantar, latero-medial, dorsolateral-palmar/plantaromedial oblique, and dorsomedial-palmar/plantarolateral oblique) with a high-frequency generator (Siemens Optitop 150/40/80, 68 kVp and 2.0 mAs) and a DR flat-panel detector (Fujifilm, FDR D-EVO II C24). Based on the post-mortem examination, limbs displaying pathological changes were excluded from the study. Subsequently, the limbs were stored at 4°C before undergoing CBCT examinations, which were conducted within 24 h after euthanasia.

2.2 | Cone beam computed tomography

The CBCT scanner utilized in this study is specifically designed and FDA-approved for use in a surgical setting (O-arm®, Medtronic Inc.). CBCT examinations were conducted under the following parameters: 120 kV, 64 mAs and a 200 mm field of view.

The fetlock region was scanned with the limbs placed in the gantry with the longitudinal axis of the foot oriented parallel to the CBCT table and perpendicular to the plane of the CBCT gantry. Initially, a native scan was conducted. Subsequently, a fetlock arthrogram was performed by injecting the joint through a dorsal approach using a 20G cannula (Stercan®, Braun). The injection consisted of a mixture of 10 mL of contrast medium containing iobitridol (Xenetix® 300, Guerbet, Sulzbach, Germany) and 10 mL of isotonic saline solution 0.9% (Braun Ecofl from B. Braun Melsungen AG), along with 1 mL of

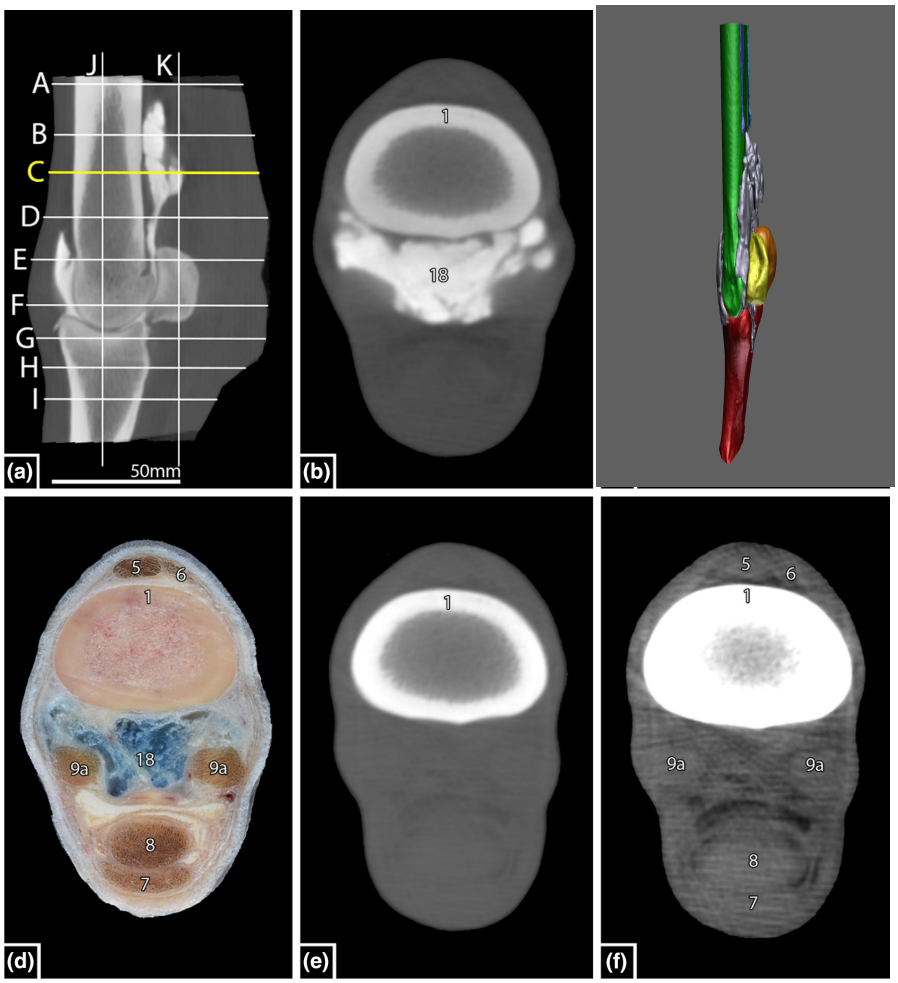

FIGURE 3 Cross-section of the fetlock joint. Illustration of the transverse sectional plane, including tendons, ligaments and bones in the area of the proximopalmar recess of the metacarpophalangeal joint. For further details, refer to the caption of Figure 1.

blue epoxy resin dye (DecorRom). To ensure an even distribution of the injected contrast solution, the fetlock joint was flexed 20 times. Subsequently, the limbs were scanned again using CBCT, with acquisition variables identical to those described for the native scans. Afterwards, the limbs were frozen at −18°C for a minimum of 48 h. A qualitative assessment of the bone and soft-tissue structures in the equine fetlock joint was performed using the acquired CBCT images.

2.3 | Gross anatomic sections

All 29 limbs were sawed using a water-cooled band saw (K440H, Kolbe Foodtec, Elchingen, Germany). Ten limbs were sectioned in the transverse plane, 10 limbs in the sagittal plane and nine limbs in the dorsal plane. The sectioned specimens were photographed (Nikon D3300 SLR-digital camera Kit AF-P 18-55 VR), and the images were edited using Photoshop (Adobe Photoshop, version 22.1.0).

2.4 | Identification of anatomic structures

CBCT scan data were rendered using a DICOM viewer program (RadiAnt, DICOM Viewer 2023.1). The bone window (WW = 3000 HU; WL = 500 HU) and the soft-tissue window (WW 600 HU; WL = 100 HU) were employed to display either native or contrast medium-enhanced CBCT images, respectively. The window width level was adjusted as required to achieve optimal images. The 3D orientation of 2D images was adjusted using a multi-planar reconstruction operation until corresponding images from gross anatomic sections were matched. Bony and soft-tissue structures were identified and annotated on paired images.

2.5 | 3D model of the fetlock region

A representative 3D model of the fetlock region was created using the Amira software program (Thermo Scientific™ Amira, version 4.6.0). Therefore, the bony structures and the fetlock joint compartment were segmented semi-automatically from a contrast medium-enhanced CBCT data set.

3 | RESULTS

Clinically relevant anatomical structures were visualized in nine transverse, two dorsal and two sagittal planes. For each plane, CBCT images (bone and soft-tissue window) with and without contrast medium were assessed in comparison with the corresponding anatomical sections (see Figures 1–13).

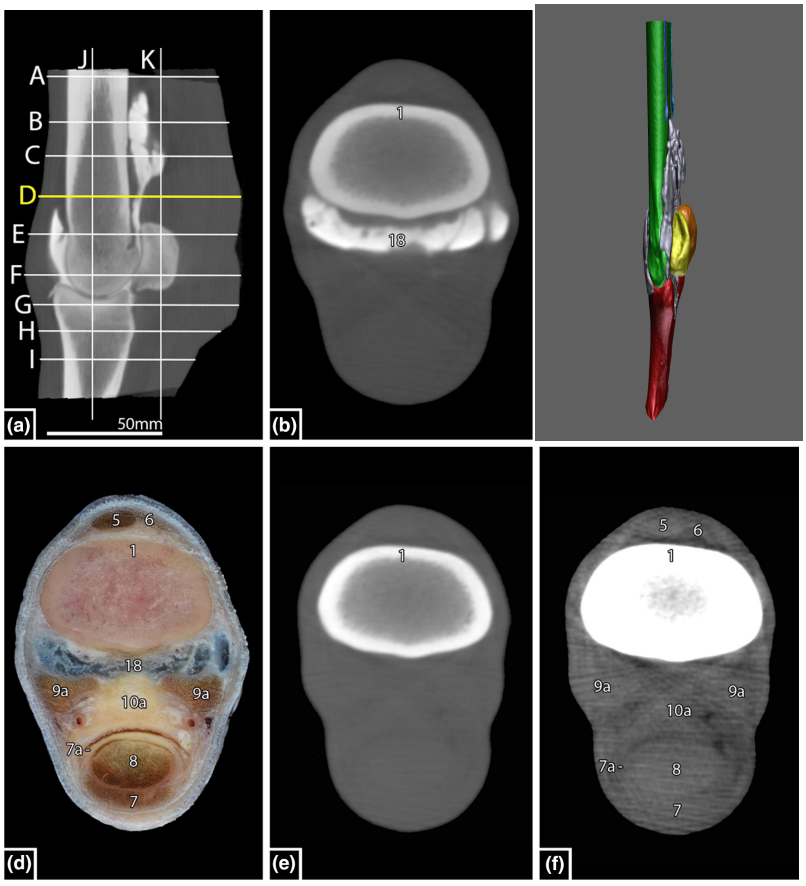

FIGURE 4 Cross-section of the fetlock joint. Illustration of the transverse sectional plane, including tendons, ligaments and bones in the area of the manica flexoria. For further details, refer to the caption of Figure 1.

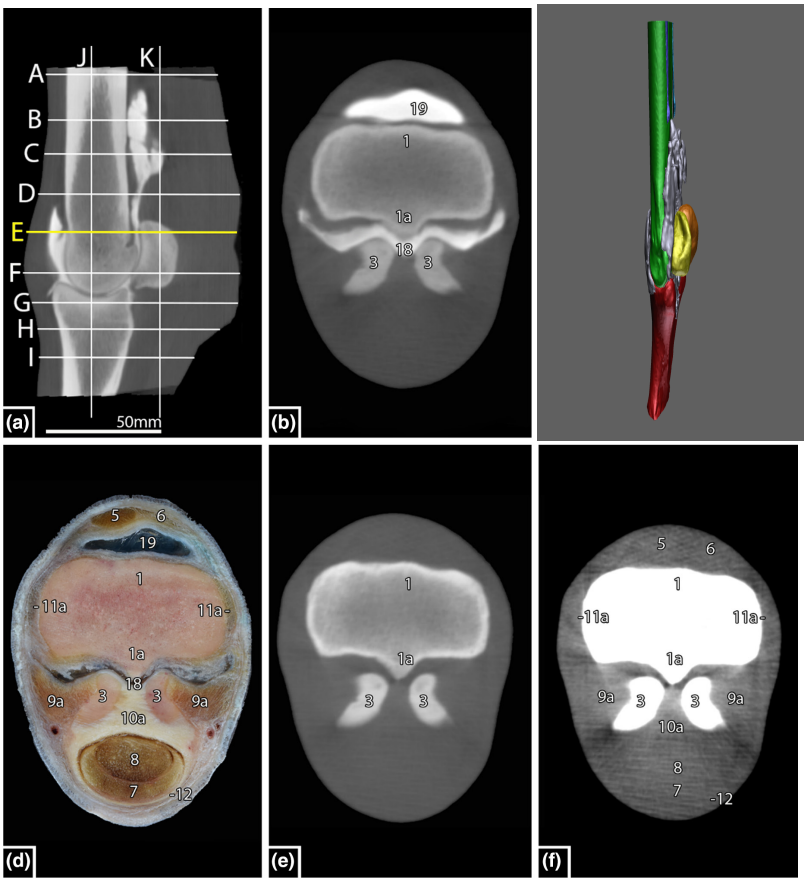

FIGURE 5 Cross-section of the fetlock joint. Illustration of the transverse sectional plane, including tendons, ligaments and bones in the area of the apex of the proximal sesamoid bones. For further details, refer to the caption of Figure 1.

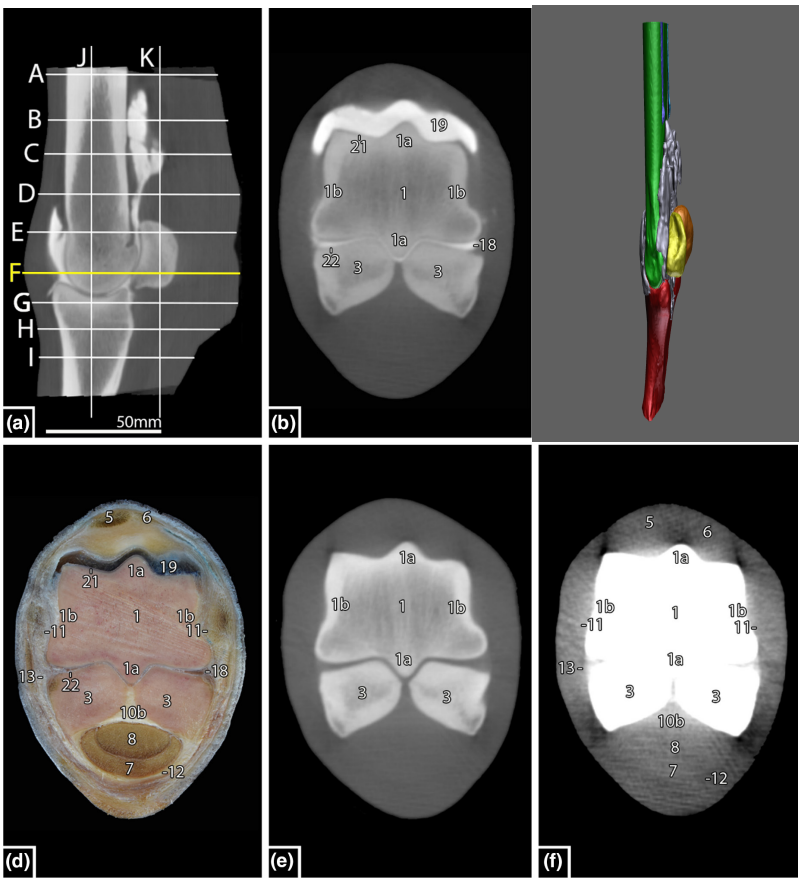

FIGURE 6 Cross-section of the fetlock joint. Illustration of the transverse sectional plane, including tendons, ligaments and bones in the area of the proximal sesamoid bones. For further details, refer to the caption of Figure 1.

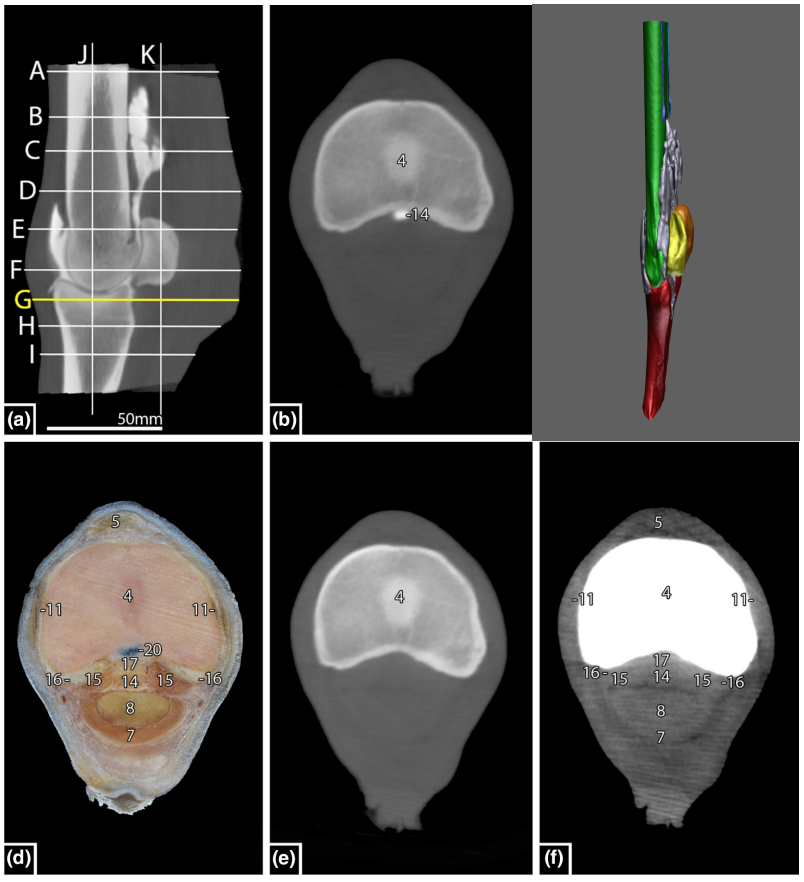

FIGURE 7 Cross-section of the fetlock joint. Illustration of the transverse sectional plane, including tendons, ligaments and bones in the area of the proximal part of the straight distal sesamoidean ligament and oblique distal sesamoidean ligaments. For further details, refer to the caption of Figure 1.

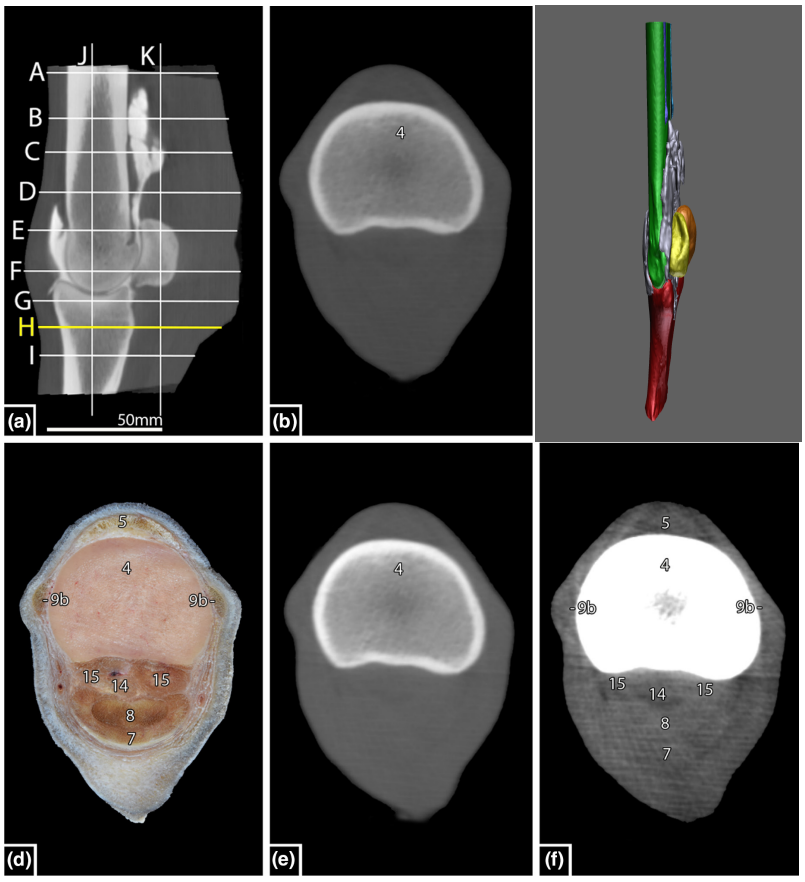

FIGURE 8 Cross-section of the fetlock joint. Illustration of the transverse sectional plane, including tendons, ligaments and bones in the area of the distal part of the oblique distal sesamoidean ligaments. For further details, refer to the caption of Figure 1.

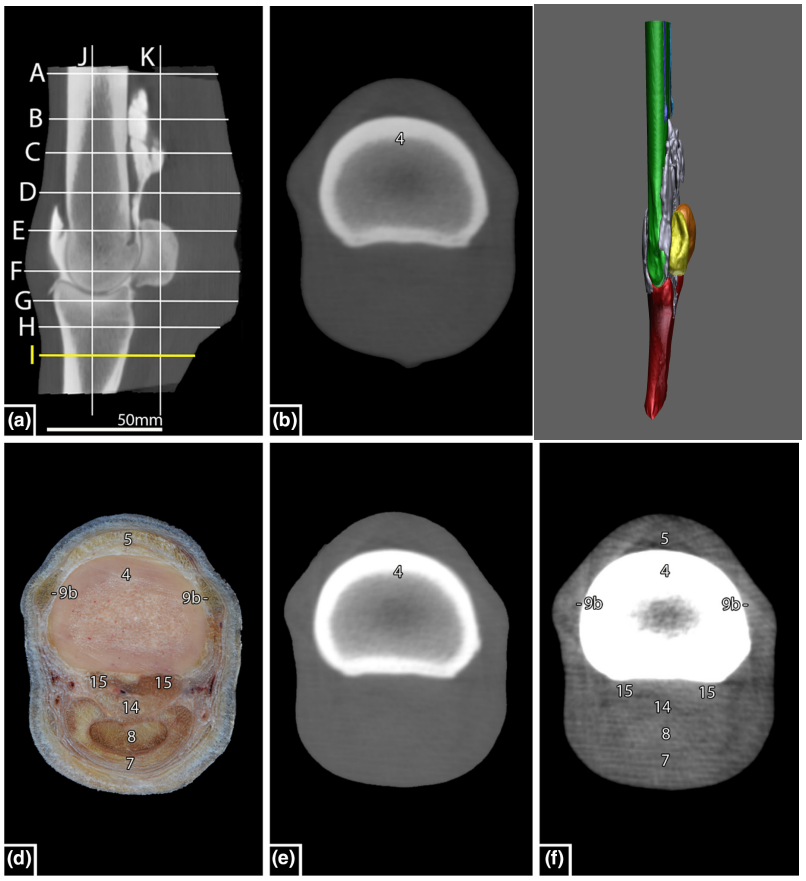

FIGURE 9 Cross-section of the fetlock joint. Illustration of the transverse sectional plane, including tendons, ligaments and bones in the area of the pastern. For further details, refer to the caption of Figure 1.

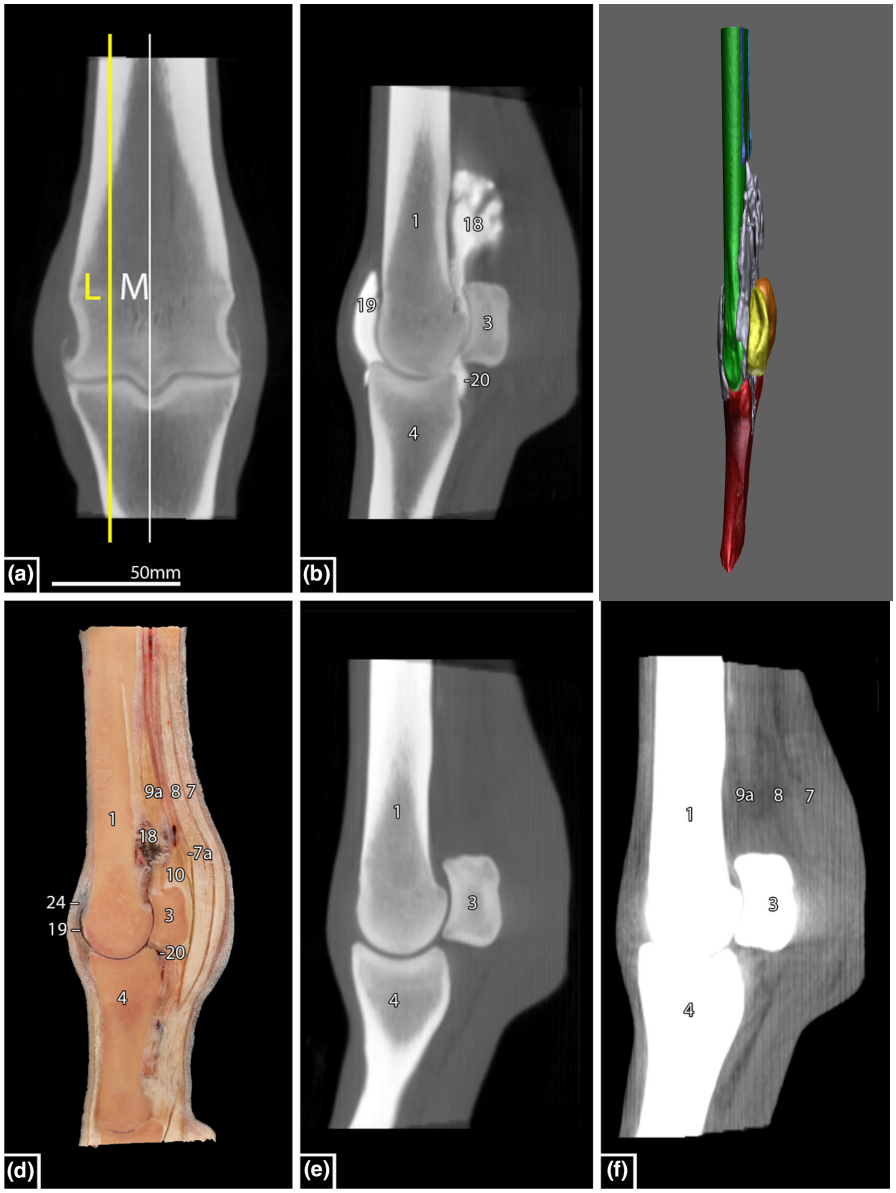

FIGURE 10 Sagittal section of the fetlock joint. Illustration of the sagittal sectional plane, including tendons, ligaments and bones in the area of the proximal sesamoid bones. For further details, refer to the caption of Figure 1.

Despite the use of fenestration, the bony structures of the fetlock joint were displayed superior to non-mineralized structures. The use of the bone window (WW = 3000 HU; WL = 500 HU) enabled us to clearly visualize the outline of the bones and to discriminate the bony compacta/cortex from the inner bony medulla (Figures 1–13). A clear delineation of the articular space of the fetlock joint was best visualized by sagittal and dorsal reconstructed images (Figures 10–13). The hyaline articular cartilage was identified as a regular, smooth, strongly attenuating line over the homogeneous, weakly attenuating subchondral bone after arthrography. The cartilage of the dorsal and palmar/plantar aspect of MCIII/MTIII and the articular surface of the proximal sesamoid bones were well identified. The cartilage at the most distal part of the sagittal ridge and the condyles of MCIII/MTIII and the cartilage of the proximal phalanx were difficult to see or were even not visible on the transverse, sagittal and dorsal planes. The extension of the synovial recesses (including the proximal synovial pad) was well identified after arthrography (Figures 2–7 and 10–13).

Soft-tissue structures were less clearly recognizable compared to bone and were also recognized differently, ranging from moderate to unrecognizable. The soft-tissue window was adjusted in the following range (WW 600 HU; WL = 100 HU).

The following structures were moderately visualized but detectable nonetheless and were identified by their location and attenuation but not by margins at the CBCT images:

- Proximal to the fetlock joint, the deep digital flexor tendon (tendon of the M. flexor digitalis profundus) had an oval shape, distally an incipient bilobed shape on the anatomical cross section (Figures 1–9d).

The following structures were poorly visualized but detectable nonetheless and were identified by location and attenuation, with clear visualization of their bony attachments:

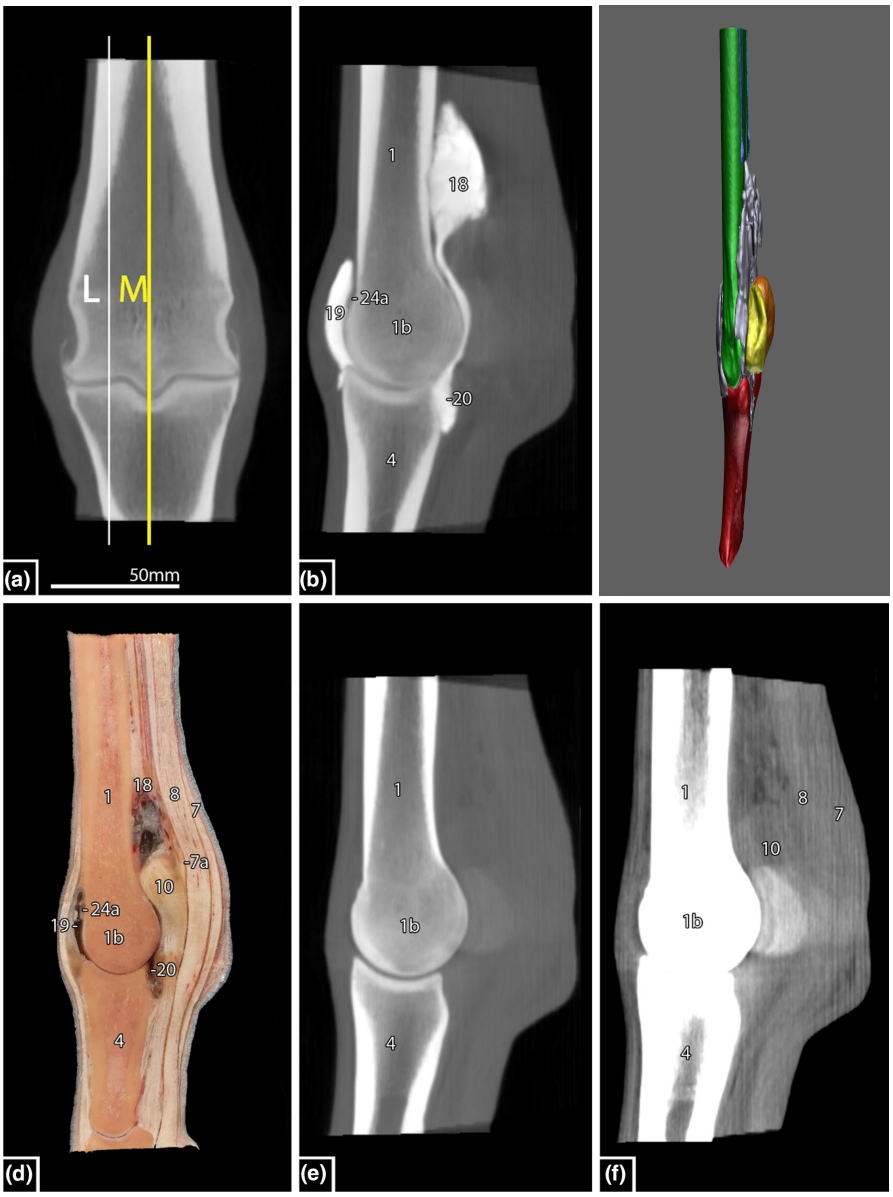

FIGURE 11 Sagittal section of the fetlock joint. Illustration of the sagittal sectional plane, including tendons, ligaments and bones in the area of the sagittal ridge of third metacarpal bone. For further details, refer to the caption of Figure 1.

- The dorsal digital extensor tendon (tendon of the M. extensor digitalis longus), appearing narrow and flat on the anatomical cross section (Figures 1–9d).
- The superficial digital flexor tendon (tendon of the M. flexor digitalis superficialis), exhibiting a flattened shape on the transverse section (Figures 1–11d).
- The lateral and medial branches of the suspensory ligament (M. interosseus medius), starting round and becoming more trapezoid-shaped as they insert at the apical and abaxial borders of the proximal sesamoid bones (Figures 1–5, 13d).
- The fibrocartilaginous intersesamoidean ligament (Lig. palmare), located between the two proximal sesamoid bones (Figures 4–6 and 13d).
- The straight distal sesamoidean ligament (Lig. sesamoideum rectum), originating from the base of the proximal sesamoid bones and the intersesamoidean ligament, and inserting distally on the second phalanx, with varying shapes along its length (Figures 7–9d).
- The oblique distal sesamoidean ligaments (Ligg. sesamoidea obliqua), with lateral, sagittal and medial parts, originating separately from the base of the medial and lateral proximal sesamoid bones and the intersesamoidean ligament, attaching on the palmar/plantar surface of the proximal phalanx to the trigonum (Trigonum phalangis proximalis) (Figures 7–9d).

The following structures were not visible, but their bony attachments were clearly visible on the CBCT images:

- The lateral and medial collateral ligaments (Lig. collaterale med./lat.), comprising superficial and deep parts, with the superficial part originating distolaterally/−medially at the metacarpal/metatarsal shaft and attaching to the proximolateral/−medial aspect of the proximal phalanx and the triangular deep part originating at the abaxial condylar fossa and inserting on the proximal phalanx and the proximal sesamoid bone (Figure 6d).

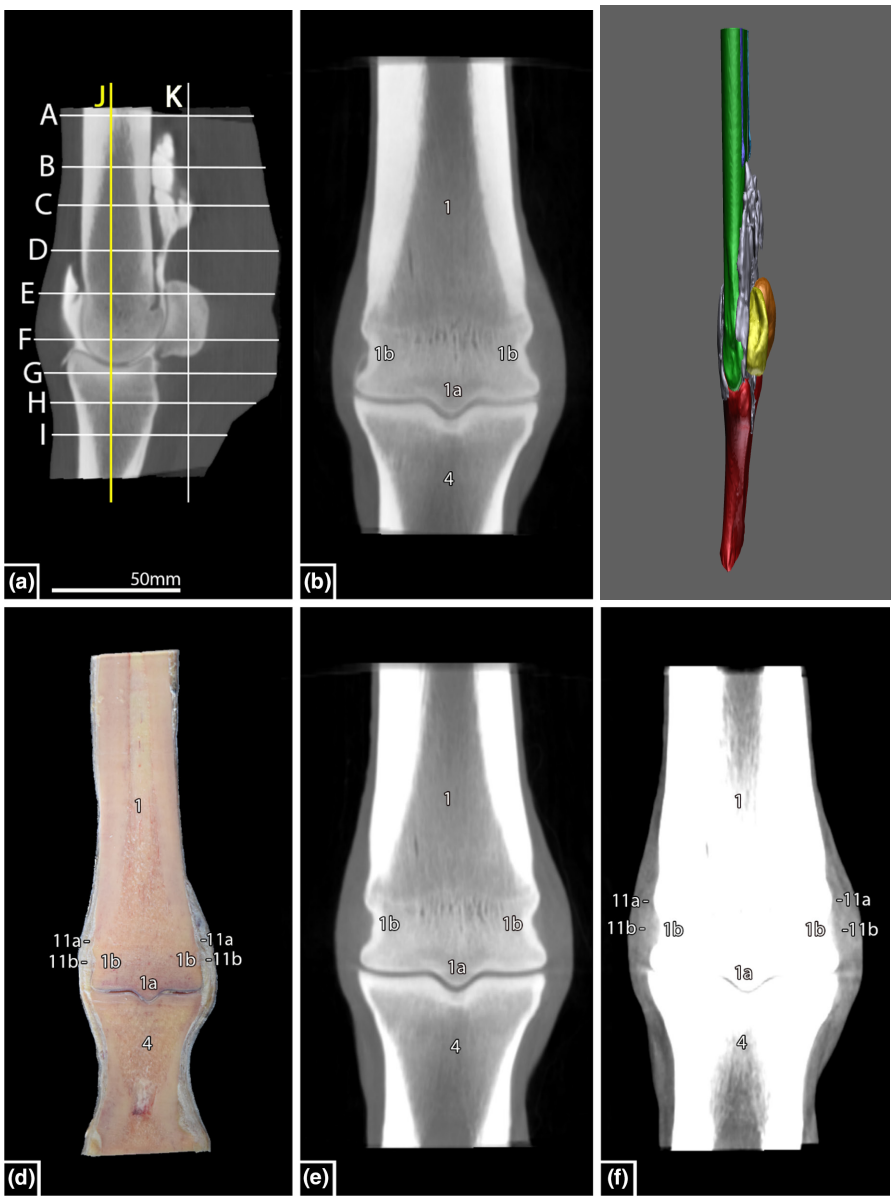

FIGURE 12 Frontal view of the fetlock joint. Illustration of the frontal sectional plane, including tendons, ligaments and bones in the area of the collateral fossa. For further details, refer to the caption of Figure 1.

- The lateral and medial collateral sesamoidean ligaments (Ligg. sesamoidea collateralia med./lat.), running from the abaxial surface of the proximal sesamoid bones to MCIII/MTIII and the tuberosity of the proximal phalanx, located superficially to the superficial part of the collateral ligaments and the extensor branches of the suspensory ligament (Figure 6d).
- The thin annular ligament (Lig. anulare palmare) positioned directly under the skin and attaching to the abaxial surfaces of the proximal sesamoid bones (Figure 6d)
- The cruciate sesamoidean ligaments (Ligg. sesamoidea cruciate), lying beneath the straight and oblique sesamoidean ligaments, crossing from the axial part of the base of the proximal sesamoid bones to the contralateral, axial aspect of the proximal phalanx, forming the palmar wall of the palmarodistal recess of the MCP/MTP joint (Figure 7d).
- The short sesamoidean ligaments (Ligg. sesamoidea brevia), extending from the dorsal aspect of the base of the proximal sesamoid bones to the palmar/plantar margin of the articular surface of the proximal phalanx (Figure 7d).

The soft-tissue structures listed below were not visible on the CBCT images:

- The manica flexoria (Manica flexoria), which originates from the superficial flexor tendon and surrounds the deep flexor tendon proximal to the MCP/MTP joint (Figure 4d).
- The metacarpo/tarsointersesamoidean ligament (Lig. metacarpo−/metatarsointersesamoideum), originating on the palmarodistal/plantarodistal aspect of MCIII/MTIII and merging with the intersesamoidean ligament

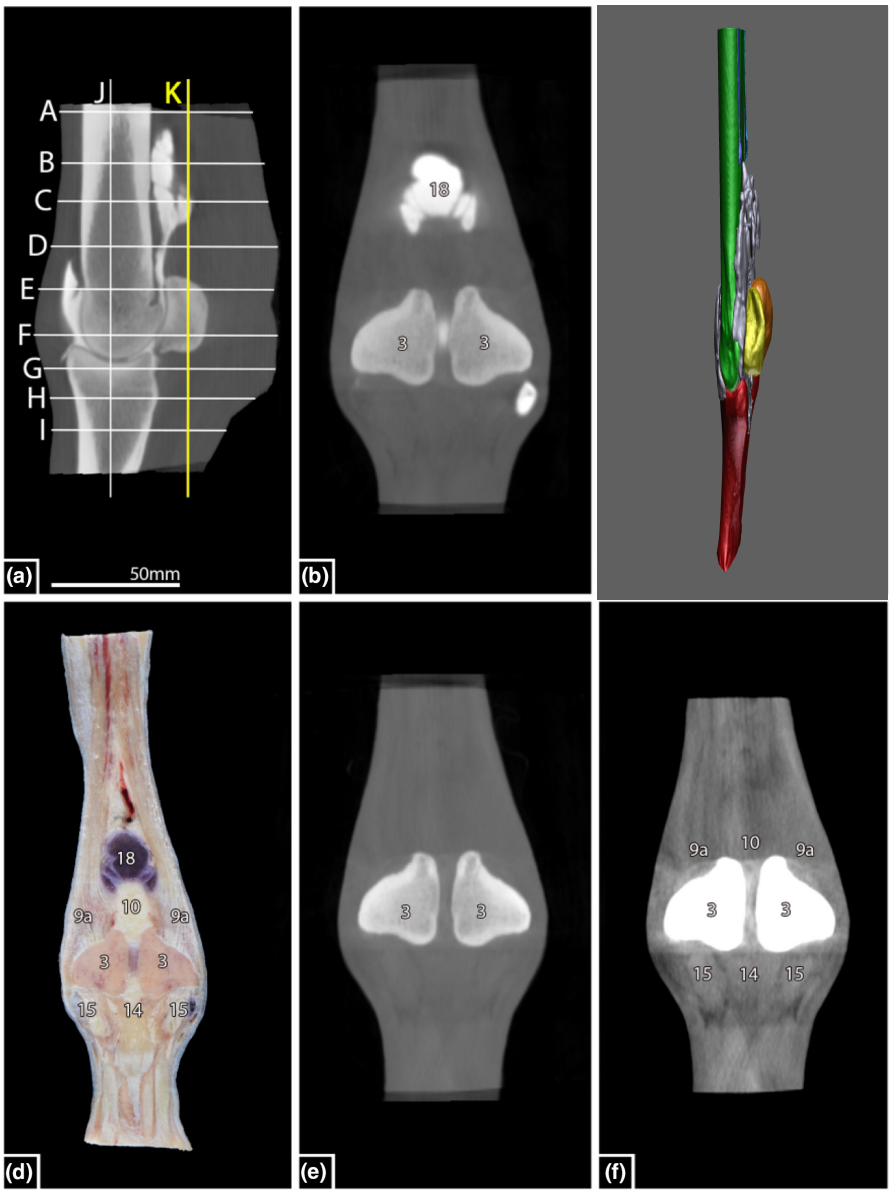

FIGURE 13 Frontal view of the fetlock joint. Illustration of the frontal sectional plane, including tendons, ligaments and bones in the area of the proximal sesamoid bones. For further details, refer to the caption of Figure 1.

4 | DISCUSSION

The objective of this study was to establish a comprehensive reference for the anatomical features of the normal MCP/MTP joint in horses using CBCT imaging. Previous research has provided a detailed multidetector computed tomography (MDCT) anatomy description of the normal MCP joint (Vanderperren et al., 2008). However, there is currently no published CBCT anatomical description specifically focusing on the fetlock joint area.

4.1 | Visualization of bony structures

The present study revealed that bony structures were clearly identified using CBCT imaging, contrasting with the less distinct visualization of soft-tissue structures. This observation aligns with results obtained in prior investigations focused on CBCT (Bierau et al., 2023; Stewart et al., 2023). CT has demonstrated its utility in diagnosing various conditions, such as subchondral bone cysts (Curtiss et al., 2021), heterotopic mineralization and adjacent pathologies in the equine fetlock region (Lin et al., 2023), as well as condylar fractures, subchondral bone lesions and small osteochondral fragments (Pauwels et al., 2021). CBCT stands out as an excellent modality for assessing bony structures. In this study, CBCT clearly illustrated the cortex and medulla of MCIII/MTIII, the proximal sesamoid bones and the proximal phalanx. The application of standing CBCT proves to be an efficient and effective screening method for evaluating subchondral bone morphology and detecting fetlock joint pathologies in young thoroughbred racehorses. Early detection facilitated by CBCT may allow for timely intervention and prevention of more severe bone injuries (Ciamillo et al., 2024).

4.2 | Visualization of soft-tissue structures

Although the visibility of soft-tissue structures can be optimized by adjusting the window settings (WW = 600 HU; WL = 100 HU), soft-tissue visualization remains inferior with CBCT compared to MDCT (Bierau et al., 2023). Nonetheless, there are software packages and technical solutions already available to further enhance soft-tissue visualization in CBCT imaging. In studies on human cadavers, a specialized soft-tissue filter (Hann filter) was utilized in CBCT imaging, resulting in significant improvement in the visualization of soft-tissue structures (Demehri et al., 2015). Some other CBCT systems used for equine medicine still have this Hann filter. The Hann filter also enabled better soft-tissue imaging in horses but was still inferior to fan beam computed tomography (FBCT) (Stewart et al., 2023). Scattered radiation from the CBCT x-ray source is a problem in CBCT imaging, particularly in the fetlock joint of horses with a high proportion of dense cortical bone and soft-tissue structures. Scattered radiation increases image noise and reduces the contrast-to-noise ratio, resulting in poorer resolution of the soft tissue (Tofts & Gore, 1980). Taking into account various image parameters (noise, scattered radiation, beam hardening, motion artefacts), it can be assumed that FBCT or MDCT will continue to outperform CBCT in the visualization of soft tissue, despite improvement through filters (Lechuga & Weidlich, 2016). A supplementary ultrasound examination is recommended due to the limited visualization of soft-tissue structures on CBCT.

4.3 | Visualization of cartilage

The MCP/MTP joint cartilage can be observed through CBCT arthrography. In our CBCT investigation, the transverse and sagittal planes proved valuable for identifying cartilage. However, visualization of the cartilage at the most distal part of the sagittal ridge and groove was challenging or not achievable in the transverse, sagittal and dorsal planes. This observation aligns with findings from previous MDCT examination studies (Vanderperren et al., 2008) and has been explained by the decrease in cartilage thickness from proximal (approx. 1 mm) to distal (approx. 0.5 mm), which leads to insufficient resolution at this level.

4.4 | Limitation

The research was performed using cadaveric limbs. To reduce artefacts resulting from post-mortem changes, the limbs were scanned as soon as possible after euthanasia, within a maximum time frame of 24 h. The scanning process for dissected limbs mimicked a scan conducted under general anaesthesia, rather than a CBCT scan performed on a standing sedated horse in which motion artefacts are more likely.

5 | CONCLUSION

The selection of the optimal imaging plane is primarily dictated by the clinical presentation. Ideally, a thorough CBCT examination of the MCP/MTP joint should include evaluation in all three planes: transverse, sagittal and dorsal reconstructions. While CBCT provides a robust assessment of the bone structures within the MCP/MTP joint, the evaluation of soft tissue is limited. To achieve a comprehensive examination, supplementary ultrasound imaging may be warranted. Consequently, a solid understanding of normal anatomy is essential, and the findings from this study can serve as a valuable reference for assessing CBCT images of equine limbs afflicted with MCP/MTP joint pathologies.

AUTHOR CONTRIBUTIONS

Jonathan Bierau: Design, investigation, acquisition of data, data analysis, interpretation, drafting of the manuscript, critical revision of the manuscript and approval of the final article. **Michael Röcken** and **Carsten Staszyk**: Design, interpretation, analysis, drafting of the manuscript, critical revision of the manuscript and approval of the final article. **Patricia Rott**: Support for the creation of the 3D animation.

ACKNOWLEDGEMENTS

The authors thank Emre Aner and Giuletta Fries for supporting the production of the anatomical sections.

CONFLICT OF INTEREST STATEMENT

The authors declare that they have no conflict of interest.

DATA AVAILABILITY STATEMENT

The data that support the findings of this study are available from the corresponding author upon reasonable request.

ORCID

Carsten Staszyk https://orcid.org/0000-0002-4973-0691

REFERENCES

Barbee, D. D., Allen, J. R., Grant, B. D., Riggs, M. W., Crawley, G. R., & Sande, R. D. (1987). Detection by computed tomography of occult osteochondral defects in the fetlock of a horse. *Equine Veterinary Journal*, *19*(6), 556–558. https://doi.org/10.1111/j.2042-3306.1987.tb02673.x

Bienert, A., & Stadler, P. (2006). Computed tomographic examination of the locomotor apparatus of horses—A review. *Pferdeheilkunde Equine Medicine*, *22*(2), 218–226. https://doi.org/10.21836/PEM20060218

Bierau, J., Cruz, A. M., Koch, C., Manso-Diaz, G., Büttner, K., Staszyk, C., & Röcken, M. (2023). Visualization of anatomical structures in the fetlock region of the horse using cone beam computed tomography in comparison with conventional multidetector computed tomography. *Frontiers in Veterinary Science*, *10*, 1278148. https://doi.org/10.3389/fvets.2023.1278148

Ciamillo, S. A., Wulster, K. B., Gassert, T. M., Richardson, D. W., Brown, K. A., Stefanovski, D., & Ortved, K. F. (2024). Prospective, longitudinal assessment of subchondral bone morphology and

pathology using standing, cone-beam computed tomography in fetlock joints of 2-year-old thoroughbred racehorses in their first year of training. *Equine Veterinary Journal*. https://doi.org/10.1111/evj.14048

Curtiss, A. L., Ortved, K. F., Dallap-Schaer, B., Gouzeev, S., Stefanovski, D., Richardson, D. W., & Wulster, K. B. (2021). Validation of standing cone beam computed tomography for diagnosing subchondral fetlock pathology in the thoroughbred racehorse. *Equine Veterinary Journal*, *53*(3), 510–523. https://doi.org/10.1111/evj.13414

Demehri, S., Muhit, A., Zbijewski, W., Stayman, J. W., Yorkston, J., Packard, N., Senn, R., Yang, D., Foos, D., Thawait, G. K., Fayad, L. M., Chhabra, A., Carrino, J. A., & Siewerdsen, J. H. (2015). Assessment of image quality in soft tissue and bone visualization tasks for a dedicated extremity cone-beam CT system. *European Radiology*, *25*(6), 1742–1751. https://doi.org/10.1007/s00330-014-3546-6

Denoix, J. M., Jacot, S., Bousseau, B., & Perrot, P. (1996). Ultrasonographic anatomy of the dorsal and abaxial aspects of the equine fetlock. *Equine Veterinary Journal*, *28*(1), 54–62. https://doi.org/10.1111/j.2042-3306.1996.tb01590.x

Hanson, J. A., Seeherman, H. J., Kirker-Head, C. A., & O'Callaghan, M. W. (1996). The role of computed tomography in evaluation of subchondral osseous lesions in seven horses with chronic synovitis. *Equine Veterinary Journal*, *28*(6), 480–488. https://doi.org/10.1111/j.2042-3306.1996.tb01621.x

Kaneps, A. J., Koblik, P. D., Freeman, D. M., Pool, R. R., & O'Brien, T. R. (1995). A comparison of radiography, computed tomography, and magnetic resonance imaging for the diagnosis of palmar process fractures in foals. *Veterinary Radiology & Ultrasound*, *36*(6), 467–477. https://doi.org/10.1111/j.1740-8261.1995.tb00298.x

Kaser-Hotz, B., Sartoretti-Schefer, S., & Weiss, R. (1994). Computed tomography and magnetic resonance imaging of the normal equine carpus. *Veterinary Radiology & Ultrasound*, *35*(6), 457–461. https://doi.org/10.1111/j.1740-8261.1994.tb02071.x

Kraft, S. L., & Gavin, P. (2001). Physical principles and technical considerations for equine computed tomography and magnetic resonance imaging. *The Veterinary Clinics of North America, Equine Practice*, *17*(1), 115–130. https://doi.org/10.1016/s0749-0739(17)30078-0

Lechuga, L., & Weidlich, G. A. (2016). Cone beam CT vs. fan beam CT: A comparison of image quality and dose delivered between two differing CT imaging modalities. *Cureus*, *8*(9), e778. https://doi.org/10.7759/cureus.778

Lin, S.-T., Peter, V. G., Schiavo, S., Pokora, R., Patrick, H., Bolas, N., Foote, A. K., Sargan, D. R., & Murray, R. C. (2023). Identification of heterotopic mineralization and adjacent pathology in the equine fetlock region by low-field magnetic resonance imaging, cone-beam and fan-beam computed tomography. *Journal of Equine Veterinary Science*, *126*, 104252. https://doi.org/10.1016/j.jevs.2023.104252

Pauwels, F. E., van der Vekens, E., Christan, Y., Koch, C., & Schweizer, D. (2021). Feasibility, indications, and radiographically confirmed diagnoses of standing extremity cone beam computed tomography in the horse. *Veterinary Surgery: VS*, *50*(2), 365–374. https://doi.org/10.1111/vsu.13560

Puchalski, S. M., Galuppo, L. D., Hornof, W. J., & Wisner, E. R. (2007). Intraarterial contrast-enhanced computed tomography of the equine distal extremity. *Veterinary Radiology & Ultrasound*, *48*(1), 21–29. https://doi.org/10.1111/j.1740-8261.2007.00198.x

Rijkenhuizen, A. B. M., van den Top, G. B., & van den Belt, A. J. M. (2005). The role of computer tomography in the surgical management of cystic lesions. *Pferdeheilkunde Equine Medicine*, *21*(4), 317–321. https://doi.org/10.21836/PEM20050408

Stewart, H. L., Siewerdsen, J. H., Nelson, B. B., & Kawcak, C. E. (2021). Use of cone-beam computed tomography for advanced imaging of the equine patient. *Equine Veterinary Journal*, *53*(5), 872–885. https://doi.org/10.1111/evj.13473

Stewart, H. L., Siewerdsen, J. H., Selberg, K. T., Bills, K. W., & Kawcak, C. E. (2023). Cone-beam computed tomography produces images of numerically comparable diagnostic quality for bone and inferior quality for soft tissues compared with fan-beam computed tomography in cadaveric equine metacarpophalangeal joints. *Veterinary Radiology & Ultrasound*, *64*(6), 1033–1036. https://doi.org/10.1111/vru.13309

Tofts, P. S., & Gore, J. C. (1980). Some sources of artefact in computed tomography. *Physics in Medicine and Biology*, *25*(1), 117–127. https://doi.org/10.1088/0031-9155/25/1/011

Tucker, R. L., & Sande, R. D. (2001). Computed tomography and magnetic resonance imaging of the equine musculoskeletal conditions. *The Veterinary Clinics of North America, Equine Practice*, *17*(1), 145–157, vii. https://doi.org/10.1016/s0749-0739(17)30080-9

Ueltschi, G., Voswinkel, K., & Lauk, H. D. (1996). Scintigraphical and radiological examination of fetlock-joints in clinically sound and lame horses. *Pferdeheilkunde Equine Medicine*, *12*(1), 25–32. https://doi.org/10.21836/PEM19960105

Vanderperren, K., Ghaye, B., Snaps, F. R., & Saunders, J. H. (2008). Evaluation of computed tomographic anatomy of the equine metacarpophalangeal joint. *American Journal of Veterinary Research*, *69*(5), 631–638. https://doi.org/10.2460/ajvr.69.5.631

Wisner, E. R., O'Brien, T. R., Pool, R. R., Pascoe, J. R., Koblick, P. D., Hornoff, W. J., & Poulos, P. W. (1991). Osteomyelitis of the axial border of the proximal sesamoid bones in seven horses. *Equine Veterinary Journal*, *23*(5), 383–389. https://doi.org/10.1111/j.2042-3306.1991.tb03743.x

Young, B. D., Samii, V. F., Mattoon, J. S., Weisbrode, S. E., & Bertone, A. L. (2007). Subchondral bone density and cartilage degeneration patterns in osteoarthritic metacarpal condyles of horses. *American Journal of Veterinary Research*, *68*(8), 841–849. https://doi.org/10.2460/ajvr.68.8.841

How to cite this article: Bierau, J., Rott, P., Röcken, M., & Staszyk, C. (2024). Cone beam computed tomography and cross-sectional anatomy of the region of the fetlock in the horse (*Equus caballus*). *Anatomia, Histologia, Embryologia*, *53*, e13079. https://doi.org/10.1111/ahe.13079